Electrically switchable quantum anomalous and spin Hall states in two-dimensional honeycomb lattices with non-Dirac bands

Sihui Wu,[1,*] Jiahui Qian,[2,3,*] Xunkai Duan,[2,3] Xianzhang Chen,[2] Zhou Cui,[2] Jiayong Zhang,[1,2,4,†] Chunlan Ma,[1,‡] and Tong Zhou[2,§]

[1]*Key Laboratory of Efficient Low-carbon Energy Conversion and Utilization of Jiangsu Provincial Higher Education Institutions, School of Physical Science and Technology, Suzhou University of Science and Technology, Suzhou 215009, China*

[2]*Eastern Institute for Advanced Study, Eastern Institute of Technology, Ningbo, Zhejiang 315200, China*

[3]*School of Physics and Astronomy, Shanghai Jiao Tong University, Shanghai 200240, China*

[4]*International Center for Quantum Design of Functional Materials (ICQD), and Hefei National Laboratory, University of Science and Technology of China, Hefei 230026, China*

(Received 5 January 2025; revised 27 April 2025; accepted 12 May 2025; published 5 June 2025)

Two-dimensional (2D) honeycomb lattices provide a versatile platform for realizing topologically nontrivial states. In this work, we uncover the coexistence and electrical tunability of quantum anomalous Hall (QAH) and quantum spin Hall (QSH) states in 2D honeycomb lattices characterized by non-Dirac band structures. Employing a tight-binding model, we demonstrate that p_x and p_y orbitals lead to quadratic non-Dirac band degeneracies at the Γ point and linear Dirac band degeneracies at the K and K′ points. The introduction of a magnetic exchange field and atomic spin-orbit coupling can induce distinct QAH and QSH gaps at separate energy levels within the same system. First-principles calculations validate these findings in a ferromagnetic monolayer of functionalized plumbene (Pb_2BrO), predicting sizable QAH (175.4 meV) and QSH (187.8 meV) gaps. Notably, the Fermi energy of monolayer Pb_2BrO resides in the QAH gap but can be electrically gated into the QSH gap, enabling reversible transitions between these two topologically nontrivial states. These results provide a theoretical foundation for the design of electrically tunable topological materials and establish 2D honeycomb lattices with non-Dirac bands as a promising platform for multifunctional quantum applications.

DOI: 10.1103/PhysRevB.111.235414

I. INTRODUCTION

Topological states of matter have emerged as a cornerstone of modern condensed-matter physics, offering new avenues for energy-efficient and dissipationless electronic technologies [1,2]. Among these, the quantum spin Hall (QSH) and quantum anomalous Hall (QAH) effects [3–6] stand out due to their robust, topologically protected edge states, which enable dissipationless spin and charge transport, respectively. These characteristics make QSH and QAH states strong candidates for next-generation spintronic and quantum devices [1–6]. The QSH effect usually arises from spin-orbit coupling (SOC)-induced band inversion [4], protected by time-reversal symmetry (TRS). While canonical models, such as the Kane-Mele [3] and Bernevig-Hughes-Zhang (BHZ) [4] frameworks, describe the QSH effect in two-dimensional (2D) honeycomb lattices with linear Dirac bands and materials like HgTe/CdTe quantum wells, recent theoretical advancements [7–9] have broadened its scope to the system with quadratic non-Dirac bands. The QAH effect, on the other hand, can be realized by introducing magnetic exchange fields to break TRS [8–15], thereby converting QSH states into spin-polarized edge states that support quantized charge transport in the absence of an external magnetic field. Numerous 2D materials have been theoretically proposed as candidates for realizing the QSH [3,16–29] and QAH [30–45] effects. Experimentally, the QSH effect has been observed in systems such as HgTe/CdTe quantum wells [46], monolayer 1T′ WTe_2 [47], and bismuthene on SiC [48]. Similarly, the QAH effect has been demonstrated in transition-metal-doped $(Bi,Sb)_2Te_3$ thin films [49,50], layered $MnBi_2Te_4$ [51], and moiré materials based on graphene and transition-metal dichalcogenides (TMDs) [52–55]. These breakthroughs have significantly advanced the field of topological quantum materials and their potential applications.

Remarkably, even in systems where TRS is broken, the QSH effect can persist as long as its spin gap [15,56–60] remains open, allowing for the coexistence of QSH and QAH states within a single material. This coexistence, although rare, presents a unique opportunity to combine spin and charge transport functionalities in multifunctional devices. Furthermore, while the gating control of electric and spin transport [61–64] has already spurred significant advancements in electronics and spintronics, achieving electrical tunability between these two topologically nontrivial states offers an unparalleled level of control over dissipationless transport. This capability could drive transformative innovations in quantum and spintronic technologies, opening new frontiers for device applications.

In this study, we investigate 2D honeycomb lattices with non-Dirac band structures as a platform for realizing

*These authors contributed equally to this work.
†Contact author: jyzhang@usts.edu.cn
‡Contact author: wlxmcl@usts.edu.cn
§Contact author: tzhou@eitech.edu.cn

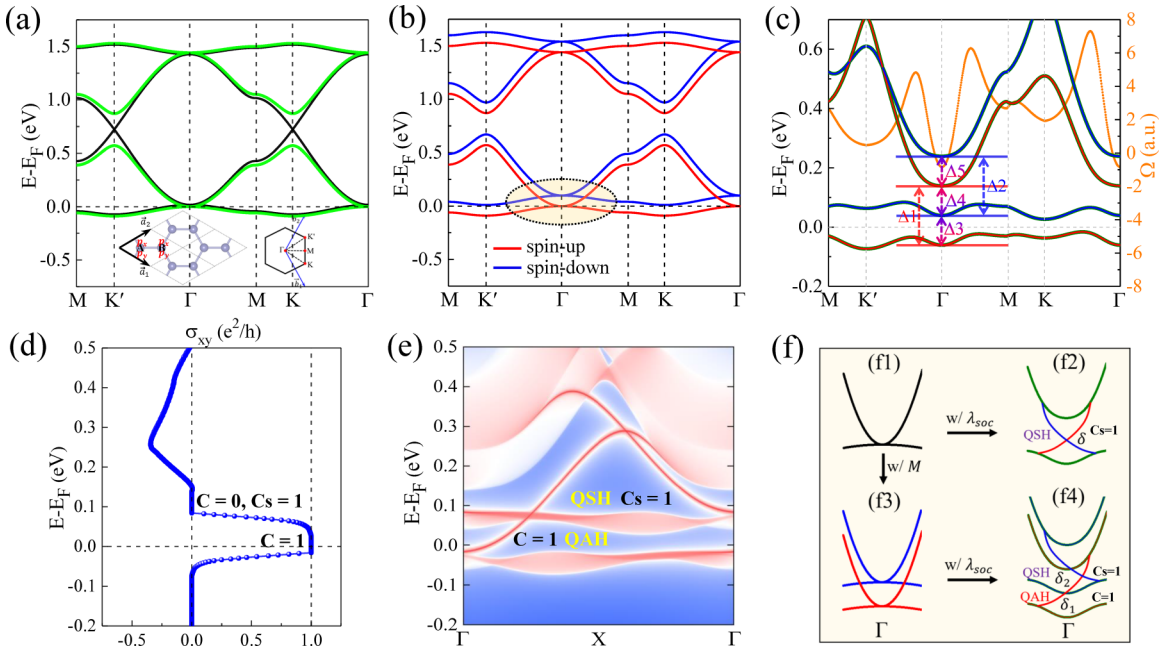

FIG. 1. Electronic band structures and topological properties obtained from the TB model for a 2D honeycomb lattice with two orbitals (p_x and p_y) per lattice site. (a) The black curves show the band structure calculated from the TB model with the parameters: $\varepsilon_{p_x} = 0.0$ eV, $\varepsilon_{p_y} = 0.0$ eV, $t_{pp\sigma} = 0.50$ eV, $t_{pp\pi} = -0.03$ eV, $U = 0.0$ eV, $M = 0.0$ eV, and $\lambda_{\rm SOC} = 0.0$ eV. The green band structure is the same as the black one, except that $U = 0.15$ eV. (left inset) A schematic illustration of the 2D honeycomb lattice with multiple p (p_x and p_y) orbitals as the basis. (right inset) The first Brillouin zone with high-symmetry points. (b) The same as the green band structure in panel (a), except that $M = 0.05$ eV. (c) The SOC bands with the projection of $\hat{s}_z$. The red and blue dots indicate the spin-up and spin-down states, respectively. The adopted TB parameters are the same as for panel (b) except that $\lambda_{\rm SOC} = 0.10$ eV. The characteristic energy gaps ($\Delta 1$ to $\Delta 5$) are marked in panel (c). The orange dots denote the calculated Berry curvatures. (d) The calculated $\sigma_{\rm xy}$ as a function of the $E_{\rm F}$ position based on the TB bands in panel (c). (e) The calculated edge states of the semi-infinite system based on the TB bands in panel (c). (f) The schematic depiction of the band evolution and topological properties of the non-Dirac bands around the Γ point, based on the TB model results in panels (a) to (e).

coexisting and electrically tunable QSH and QAH states. Through tight-binding (TB) model calculations, we show that p_x and p_y orbitals in these lattices produce quadratic non-Dirac degeneracies at the Γ point and linear Dirac degeneracies at the K and K′ points in the absence of SOC. Upon introducing atomic SOC and a magnetic exchange field, substantial QSH and QAH gaps emerge around the non-Dirac Γ point. We focus on functionalized plumbene (Pb_2BrO), a ferromagnetic (FM) monolayer material predicted to exhibit a QAH gap of 175.4 meV and a QSH gap of 187.8 meV. Crucially, the material's Fermi energy $E_{\rm F}$ lies within the QAH gap but can be shifted into the QSH gap through electrical gating, facilitating reversible transitions between these two topologically nontrivial states. These findings underscore the transformative potential of 2D honeycomb lattices with non-Dirac bands in the development of tunable quantum materials for versatile topological applications.

II. RESULTS AND DISCUSSION

A. Electrically switchable QAH and QSH states: TB model analysis

The left inset in Fig. 1(a) shows a schematic drawing of a 2D honeycomb lattice with two nonequivalent A and B sublattices. We now study the novel electronic structures and topological properties of this 2D honeycomb lattice with multiple p (p_x and p_y) orbitals at the A and B sites. The total TB model Hamiltonian of this 2D honeycomb lattice, in the basis of (p_{Ax}, p_{Ay}, p_{Bx}, p_{By}) can be written as

$$H(k) = H_{\rm hop}(k) + H_{\rm SOC} + H_{\rm U} - H_{\rm M} = \begin{bmatrix} H_{\rm hop\uparrow} & 0 \\ 0 & H_{\rm hop\downarrow} \end{bmatrix} + \begin{bmatrix} H_{\rm SOC\uparrow} & 0 \\ 0 & H_{\rm SOC\downarrow} \end{bmatrix} + \begin{bmatrix} U\mathbf{I} & 0 & 0 & 0 \\ 0 & -U\mathbf{I} & 0 & 0 \\ 0 & 0 & U\mathbf{I} & 0 \\ 0 & 0 & 0 & -U\mathbf{I} \end{bmatrix} - \begin{bmatrix} M\mathbf{I} & 0 & 0 & 0 \\ 0 & M\mathbf{I} & 0 & 0 \\ 0 & 0 & -M\mathbf{I} & 0 \\ 0 & 0 & 0 & -M\mathbf{I} \end{bmatrix}, \quad (1)$$

where $H_{\rm hop}$, $H_{\rm SOC}$, $H_{\rm U}$, and $H_{\rm M}$ represent the nearest-neighbor (NN) hopping term, the atomic SOC term, the staggered AB-sublattice potential term, and the magnetic exchange field term, respectively. The up and down arrows denote the spin-up and spin-down channels, respectively. U represents the staggered sublattice potential strength between the A and B sublattices. M denotes the applied exchange field strength at the A and B sites. The $\mathbf{I}$ in Eq. (1) is the 2×2 unit matrix.

The hopping term for the spin-up and spin-down channels can be expressed as

$$H_{\rm hop\uparrow} = H_{\rm hop\downarrow} = \begin{bmatrix} H^{AA} & H^{AB} \\ H^{BA} & H^{BB} \end{bmatrix}, \tag{2}$$

where the diagonal matrix elements represent the on-site energies for the two orbitals (p_x and p_y), and A and B refer to the nonequivalent A and B sites in the unit cell. H^{AA} and H^{BB} can be written as

$$H^{AA} = H^{BB} = \begin{bmatrix} \varepsilon_{p_x} & 0 \\ 0 & \varepsilon_{p_y} \end{bmatrix}, \tag{3}$$

where ε_{p_x} and ε_{p_y} are the on-site energies for the p_x and p_y orbitals, respectively. The off-diagonal block matrices H^{AB} and H^{BA} represent the hopping interactions between the A and B sites. The H^{AB} and H^{BA} can be written as

$$H^{AB} = \begin{bmatrix} h^{AB}_{xx} & h^{AB}_{xy} \\ h^{AB}_{yx} & h^{AB}_{yy} \end{bmatrix}, \quad H^{BA} = \left(H^{AB}\right)^{\dagger}, \tag{4}$$

in which

$$\begin{aligned} h^{AB}_{xx} &= e^{ik_x} t_{pp\sigma} + e^{i\left(-\frac{1}{2}k_x\right)} \cos\left(\frac{\sqrt{3}}{2}k_y\right)\left[\frac{1}{2}t_{pp\sigma} + \frac{3}{2}t_{pp\pi}\right], \\ h^{AB}_{xy} &= \frac{\sqrt{3}i}{2} e^{i\left(-\frac{1}{2}k_x\right)} \sin\left(\frac{\sqrt{3}}{2}k_y\right)[t_{pp\pi} - t_{pp\sigma}], \\ h^{AB}_{yy} &= e^{ik_x} t_{pp\pi} + e^{i\left(-\frac{1}{2}k_x\right)} \cos\left(\frac{\sqrt{3}}{2}k_y\right)\left[\frac{3}{2}t_{pp\sigma} + \frac{1}{2}t_{pp\pi}\right], \\ h^{AB}_{yx} &= h^{AB}_{xy}, \end{aligned} \tag{5}$$

where $t_{pp\sigma}$ and $t_{pp\pi}$ are the NN hopping parameters corresponding to the σ and π bonds formed by p_x and p_y orbitals.

The atomic SOC terms of this 2D honeycomb lattice do not include the coupling between the different spin components, indicating that the spin-up and spin-down channels are decoupled. For each spin channel, the atomic SOC can be written as

$$H_{\rm SOC\uparrow/\downarrow} = s \cdot \lambda_{\rm SOC} \begin{bmatrix} 0 & -i & 0 & 0 \\ i & 0 & 0 & 0 \\ 0 & 0 & 0 & -i \\ 0 & 0 & i & 0 \end{bmatrix}, \tag{6}$$

where $\lambda_{\rm SOC}$ is the atomic SOC strength of the A and B sites, and $s = +1$ and -1 represent the spin-up and spin-down channels, respectively.

The band structures of the 2D honeycomb lattice with two orbitals (p_x and p_y) per lattice site, calculated using the above constructed TB model Hamiltonian, are presented in Fig. 1. The black curves in Fig. 1(a) show the TB band structure calculated using the following parameters: $\varepsilon_{p_x} = 0.0$ eV, $\varepsilon_{p_y} = 0.0$ eV, $t_{pp\sigma} = 0.50$ eV, $t_{pp\pi} = -0.03$ eV, $U = 0.0$ eV, $M = 0.0$ eV, and $\lambda_{\rm SOC} = 0.0$ eV, with only the NN hopping term considered. As illustrated in the black curves in Fig. 1(a), the multiple p (p_x and p_y) bands are not only degenerate at the Γ point with quadratic non-Dirac band dispersion but also degenerate at the K and K′ points with linear Dirac band dispersion. Theoretical studies [3,7–10] show that bands without SOC, degenerate at the non-Dirac Γ point or the Dirac K and K′ points, are important for realizing topologically nontrivial states. When the staggered AB-sublattice potential U is taken into account, the degeneracies at the Dirac K and K′ points are eliminated, while the degeneracy at the non-Dirac Γ point is preserved, as shown in the green band structure in Fig. 1(a) with $U = 0.15$ eV. This indicates that the non-Dirac degeneracy at the Γ point in this TB model remains robust against the staggered sublattice potential. If atomic SOC is further considered, the degeneracy at the non-Dirac Γ point is eliminated, and a band gap opens around the Γ point, as illustrated in Fig. S1(b) with $\lambda_{\rm SOC} = 0.10$ eV in the Supplemental Material (SM) [65]. This atomic SOC-induced band gap corresponds to a QSH state, as evinced by the calculated edge states given in Fig. S1(c) in the SM [65], which include two (spin-up and spin-down) topologically nontrivial edge states connecting the valence and conduction bands.

Figure 1(b) shows the corresponding band structure of the green one of Fig. 1(a) by further considering a magnetic exchange field of $M = 0.05$ eV, in which the spin-up and spin-down bands are spin-split. In Fig. 1(b), the degenerate points of the spin-up and spin-down non-Dirac bands at the Γ point are separated. When atomic SOC is included, the degeneracies of the spin-up and spin-down quadratic non-Dirac bands are all removed and energy gaps around the Γ point are opened. Figure 1(c) plots a magnified view of the band structure from Fig. 1(b) near the $E_{\rm F}$, incorporating an atomic SOC strength of $\lambda_{\rm SOC} = 0.10$ eV. The different colors in the SOC band structure in Fig. 1(c) express the projection of the spin operator $\hat{s}_z$, i.e., $\langle\psi_{n\mathbf{k}}|\hat{s}_z|\psi_{n\mathbf{k}}\rangle$, red and blue colors indicate the spin-up and spin-down states, respectively. In Fig. 1(c), $\Delta 1$ and $\Delta 2$ denote the SOC-induced energy gaps at the Γ point, corresponding to the spin-up and spin-down non-Dirac degenerate points shown in Fig. 1(b), respectively. For the SOC bands in Fig. 1(c), the energy gaps of $\Delta 1$ and $\Delta 2$ overlap, resulting in three typical energy gaps: $\Delta 3$, $\Delta 4$, and $\Delta 5$, as denoted in Fig. 1(c).

The Berry curvatures $\Omega(\mathbf{k})$, Chern numbers, and edge states are calculated to identify the topological properties of the three energy gaps $\Delta 3$, $\Delta 4$, and $\Delta 5$ in the SOC band structure in Fig. 1(c). The Berry curvatures are calculated by [66,67]

$$\Omega(\mathbf{k}) = \sum_n f_n \Omega_n(\mathbf{k}), \tag{7}$$

$$\Omega_n(\mathbf{k}) = -2\,\mathrm{Im} \sum_{m \neq n} \frac{\hbar^2 \langle\psi_{n\mathbf{k}}|v_x|\psi_{m\mathbf{k}}\rangle\langle\psi_{m\mathbf{k}}|v_y|\psi_{n\mathbf{k}}\rangle}{(\mathrm{E}_m - \mathrm{E}_n)^2}, \tag{8}$$

where f_n is the Fermi-Dirac distribution function, $v_{x(y)}$ are the velocity operators, E_n is the eigenvalue of the Bloch functions $|\psi_{n\mathbf{k}}\rangle$, and the summation is over all of the occupied states. The Chern number C can be obtained by integrating the $\Omega(\mathbf{k})$ over the first Brillouin zone (BZ), as $C = \frac{1}{2\pi}\sum_n \int_{BZ} d^2k \Omega_n$. The orange dots in Fig. 1(c) display the calculated $\Omega(\mathbf{k})$

of the SOC band structure, with the E_F located within the global band gap associated with the energy gap $\Delta 3$. We can observe that the large values of the obtained $\Omega(\mathbf{k})$ are mainly distributed around the non-Dirac Γ point, forming an approximate M shape. By integrating the $\Omega(\mathbf{k})$ over the first BZ, the nonzero integer Chern number of $C = 1$ is obtained, indicating the global insulating state inside $\Delta 3$ in Fig. 1(c) is the QAH state. Figure 1(d) plots the calculated anomalous Hall conductivity σ_{xy} as a function of the E_F position, showing that the quantized σ_{xy} with $C = 1$ appears around the original E_F. When E_F is tuned to the global insulating state inside the energy gap $\Delta 4$ in Fig. 1(c), the Chern numbers of $C = 0$ are obtained, as shown in Fig. 1(d), indicating this insulating state is not a QAH state. In addition, when E_F is further tuned to the energy gap $\Delta 5$ in Fig. 1(c), the negative noninteger Chern numbers ($C < 0$) are obtained, as there is no global insulating state in $\Delta 5$. By integrating the $\Omega(\mathbf{k})$, obtained when E_F is located within $\Delta 5$, around the non-Dirac Γ point, the nonzero integer Chern number of $C = -1$ is obtained, implying that the local energy gap $\Delta 5$ around the Γ point is a QAH state with $C = -1$.

Furthermore, if the SOC-induced energy gaps $\Delta 1$ and $\Delta 2$ in Fig. 1(c) are completely separate, as shown in Fig. S2(b) in SM [65] under a large exchange field of $M = 1.20$ eV, the energy gaps $\Delta 1$ and $\Delta 2$ correspond to the QAH states with Chern numbers $C_\uparrow = 1$ and $C_\downarrow = -1$, respectively, as illustrated in Figs. S2(e) and S2(f) in the SM [65]. Since energy gap $\Delta 4$ arises from the overlap between $\Delta 1$ and $\Delta 2$, its Chern number becomes $C = C_\uparrow + C_\downarrow = 0$. However, the spin Chern number for $\Delta 4$ is given by $C_S = \frac{1}{2}(C_\uparrow - C_\downarrow) = 1$, indicating that $\Delta 4$ in Fig. 1(c) corresponds to a QSH state. The density of states of the semi-infinite system, corresponding to the SOC bands in Fig. 1(c), is plotted in Fig. 1(e). It reveals one (spin-up) topologically nontrivial edge states within the energy gap $\Delta 3$ and two (spin-up and spin-down) topologically nontrivial edge states within the energy gap $\Delta 4$, confirming that $\Delta 3$ corresponds to a QAH state and $\Delta 4$ to a QSH state. The phase diagrams depicting the evolution of topological states as functions of the magnetic exchange field M and atomic SOC λ_{SOC} for the energy gaps $\Delta 3$ and $\Delta 4$ shown in Fig. 1(c) are presented in Fig. S3 in the SM [65].

Excitingly, using our constructed TB model for 2D honeycomb lattices with multiple p (p_x and p_y) orbitals, we demonstrate that introducing an appropriate magnetic exchange field and atomic SOC can simultaneously open QAH and QSH gaps around the non-Dirac Γ point. Notably, these two topologically nontrivial states can be switched by tuning the chemical potential though an electrical gate. To illustrate the mechanism for simultaneously achieving QAH and QSH gaps in a single material system from a physical perspective, we present a schematic diagram of band evolution and its topological properties in Fig. 1(f). The red and blue curves in Figs. 1(f2) and 1(f4) represent the spin-up and spin-down edge states at one edge of the sample, respectively. As shown in Fig. 1(f1), the band structure exhibits a quadratic non-Dirac degenerate point at the Γ point. Introducing atomic SOC enables the system to realize the QSH state, as depicted in Fig. 1(f2). When a magnetic exchange field is applied to the system in Fig. 1(f1), the non-Dirac degenerate point at the Γ point undergoes spin splitting, as illustrated in Fig. 1(f3). By further incorporating atomic SOC, both QAH and QSH gaps can be simultaneously opened at the Γ point. In the following section, we use a FM monolayer of functionalized plumbene (Pb_2BrO) as a concrete example to demonstrate that the remarkable topological properties, featuring both QAH and QSH gaps within a single system, as predicted by our TB model, can indeed be realized in realistic 2D material systems.

B. Electrically switchable QAH and QSH states in functionalized plumbene

The first-principles calculations are performed by using the projected augmented wave (PAW) [68] formalism based on density functional theory (DFT), as implemented in the Vienna *ab initio* Simulation Package (VASP) [69]. The Perdew-Burke-Ernzerhof generalized gradient approximation (GGA-PBE) is employed to describe the exchange and correlation functional [70]. The plane-wave energy cutoff and the total-energy convergence criterion are set to be 550 eV and 10^{-6} eV, respectively. A vacuum space greater than 15 Å is employed to prevent interactions between adjacent slabs. All atoms in the unit cell are allowed to relax until the Hellmann-Feynman force on each atom is less than 0.01 eV/Å. The $16 \times 16 \times 1$, $8 \times 16 \times 1$, and $9 \times 9 \times 1$ Gamma central Monkhorst-Pack grids are used in the calculations for the $1 \times 1 \times 1$ unit cell, $2 \times 1 \times 1$ supercell, and $\sqrt{3} \times \sqrt{3} \times 1$ supercell of the monolayer functionalized plumbene. The Monte Carlo (MC) simulations based on the classical two-dimensional (2D) Heisenberg model are performed to estimate the Curie temperature T_C. To investigate the topological properties of the functionalized plumbene, the maximally localized Wannier functions (MLWFs) [71,72] are constructed using the WANNIER90 package [73]. The Berry curvatures, anomalous Hall conductivity, and Chern numbers are calculated by employing the algorithm described in Ref. [74]. The edge states of the semi-infinite system are calculated using the WANNIERTOOLS package [75].

The crystal structure of monolayer functionalized plumbene Pb_2BrO, which is generated by uniformly functionalizing the monolayer plumbene thin film with Br and O atoms on its two opposite surfaces, is illustrated in Fig. 2(a). The unit cell of monolayer Pb_2BrO, along with lattice vectors $\vec{a}_1$ and $\vec{a}_2$, is denoted in Fig. 2(a). This unit cell contains two Pb atoms, one Br atom, and one O atom. Specifically, the Pb atoms form a 2D honeycomb lattice, whereas the Br(O) atoms form a 2D triangular lattice. The optimized equilibrium lattice constant of the monolayer Pb_2BrO is $a = 5.67$ Å. The first BZ with reciprocal-lattice vectors $\vec{b}_1$ and $\vec{b}_2$ and high-symmetry points are given in the inset in Fig. 2(a). Owing to the presence of unbonded p_z orbitals on the Pb atoms in pristine monolayer plumbene, adatoms are energetically favorable to adsorb and bond with these Pb atoms. To evaluate the structural stability of the functionalized plumbene Pb_2BrO, we calculate its adsorption energy. The adsorption energy is defined as $E_{ads} = E(\text{plumbene}) + E(\text{adatom}) - E(\text{adatom} - \text{plumbene})$, where $E(\text{plumbene})$, $E(\text{adatom})$, and $E(\text{adatom} - \text{plumbene})$ represent the total energies of pristine plumbene, isolated adatom, and adatom-plumbene system, respectively. The calculated adsorption energy of Br and O atoms adsorbed on

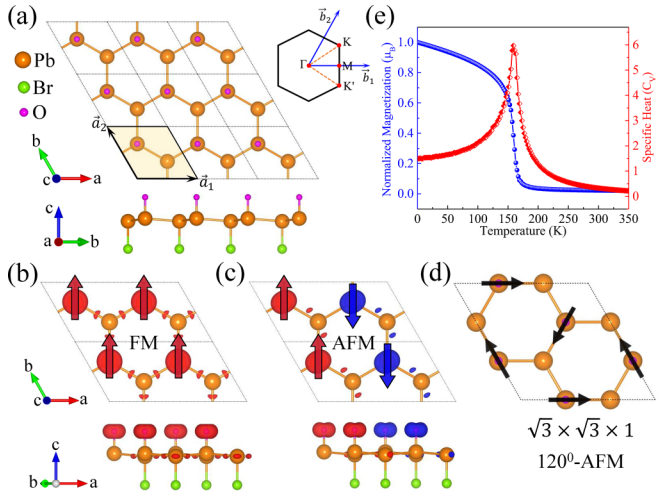

FIG. 2. (a) Top and side views of the atomic structure of monolayer Pb_2BrO. The rhombus in panel (a) shows the unit cell with lattice vectors $\vec{a}_1$ and $\vec{a}_2$. The inset in panel (a) shows the first BZ with high-symmetry points. (b), (c) Spatial spin-density distributions $(\rho_\uparrow - \rho_\downarrow)$ for the top and side views of the FM (b) and collinear AFM (c) magnetic configurations. The red and blue arrows denote the up and down spins, respectively. (d) The noncollinear 120°-AFM magnetic configuration. The black arrows in panel (d) denote the noncollinear spins that lie in the 2D plane. (e) Temperature dependence of the normalized magnetic moment and special heat capacity of monolayer Pb_2BrO obtained from MC simulations.

pristine plumbene is found to be 5.77 eV, indicating strong binding and suggesting robust structural stability of the functionalized plumbene Pb_2BrO. Notably, Janus-graphene, a nonsymmetrically functionalized form of graphene, has been experimentally synthesized via a two-step surface covalent functionalization process [76], suggesting the feasibility of synthesizing a similar Janus-type structure in the Pb_2BrO monolayer. Based on the analysis utilizing the TB model, the inclusion of a magnetic exchange field within the targeted materials is necessary to realize the QAH and QSH gaps simultaneously in single materials. Thus, the magnetic properties of monolayer Pb_2BrO are critical for the realization of the proposed exceptional topologically nontrivial states.

Our first-principles calculations reveal that the FM state is more stable than the nonmagnetic (NM) state by 61.10 meV per unit cell, suggesting a preferential stabilization of the spin-polarized state in monolayer Pb_2BrO. For the FM state, the unit cell possesses a net magnetic moment of $1.0\mu_B$. This net magnetic moment arises predominantly from the localized electrons on the O atoms, as evident from the calculated spin-density distribution depicted in Fig. 2(b). To examine the magnetic ground state of monolayer Pb_2BrO, we consider the following three prototypical magnetic configurations of the 2D triangular lattice: FM, collinear antiferromagnetic (AFM), and noncollinear 120° AFM, as illustrated in Figs. 2(b)– 2(d). Our calculations demonstrate that the magnetic ground state of monolayer Pb_2BrO is in the FM state, which is more stable than the collinear AFM state and noncollinear 120°-AFM state by 32.34 and 52.94 meV per unit cell, respectively. The magnetic anisotropy energy (MAE) is a key parameter for 2D magnetic materials. For monolayer Pb_2BrO in the FM state, the MAE per O atom is calculated using the expression: $\text{MAE} = E_{[100]} - E_{[001]}$, where $E_{[100]}$ and $E_{[001]}$ represent the total energies of the FM state monolayer Pb_2BrO with magnetization along the [100] and [001] directions, respectively. The [100] direction is parallel to the 2D monolayer plane, while the [001] direction is perpendicular to it. The [100] and [001] directions are along the $a(x)$ and $c(z)$ directions shown in Fig. 2(a). The calculated MAE is found to be 17.47 meV/O, significantly exceeding that of the monolayer CrI_3, which is reported as 0.686 meV/Cr [77]. The obtained positive value of MAE (MAE >0) indicate that the easy axis of the monolayer Pb_2BrO is the out-of-plane direction.

For monolayer Pb_2BrO, the nearest-neighbor (NN) exchange interaction parameter can be extracted by mapping the total energy of the system with two distinct magnetic configurations, FM [Fig. 2(b)] and AFM [Fig. 2(a)], to the Heisenberg spin Hamiltonian on a 2D triangular lattice:

$$H = -J_1 \sum_{\langle ij \rangle} \vec{S}_i \cdot \vec{S}_j - D \sum_i \left|\vec{S}_i^z\right|^2, \tag{9}$$

where J_1 represents the exchange interactions between NN spins, $\vec{s}_i^z$ denotes the spin component along the z axis, and D signifies the uniaxial anisotropy energy. The parameters J_1 and D in Eq. (9) can be obtained from the following equations:

$$E_{\text{FM}} = E_0 - 6J_1|\vec{S}|^2, \quad E_{\text{AFM}} = E_0 + 2J_1|\vec{S}|^2,$$
$$D = \frac{\text{MAE}}{|\vec{S}|^2}, \tag{10}$$

where E_0 is the ground-state energy, independent of the spin configurations. Thus, the NN exchange interaction energy is calculated as $J_1 = (E_{\text{AFM}} - E_{\text{FM}})/(8|\vec{S}|^2)$. E_{FM} and E_{AFM} represent the total energies of the $2 \times 1 \times 1$ supercell monolayer Pb_2BrO in the FM and AFM states, respectively. Here, the spin $|\vec{S}|$ is set to 1.0 ($|\vec{S}| = 1.0$). The value of J_1 is positive for FM materials and negative for AFM materials. The calculated exchange interaction parameter J_1 for monolayer Pb_2BrO is 8.09 meV. Using the exchange interaction parameters J_1 and D obtained from DFT calculations, the Curie temperature T_C for the monolayer Pb_2BrO in the FM state is estimated through Monte Carlo (MC) simulations. These simulations are based on the classical anisotropy 2D Heisenberg model using the Metropolis algorithm. A $60 \times 60 \times 1$ 2D triangular lattice is employed, and 5×10^5 steps are performed for each temperature. The temperature-dependent normalized magnetic moment and specific heat capacity C_V are plotted in Fig. 2(e), from which an estimated T_C of 160 K can be observed.

Figure 3(a) shows the calculated spin-polarized band structure of the monolayer Pb_2BrO in its FM magnetic ground state, from which we can observe that the quadratic non-Dirac band degeneracies at the Γ point, in proximity to E_F, exhibit spin splitting. The spin-polarized non-Dirac bands, as indicated by the yellow-shaded area in Fig. 3(a) from DFT calculations, display the same character as those in the corresponding yellow-shaded area of Fig. 1(b), which are derived from our TB model calculations. Figure 3(b) displays the orbital-resolved band structure of Fig. 3(a), with the orange and violet dots corresponding to contributions from the Pb

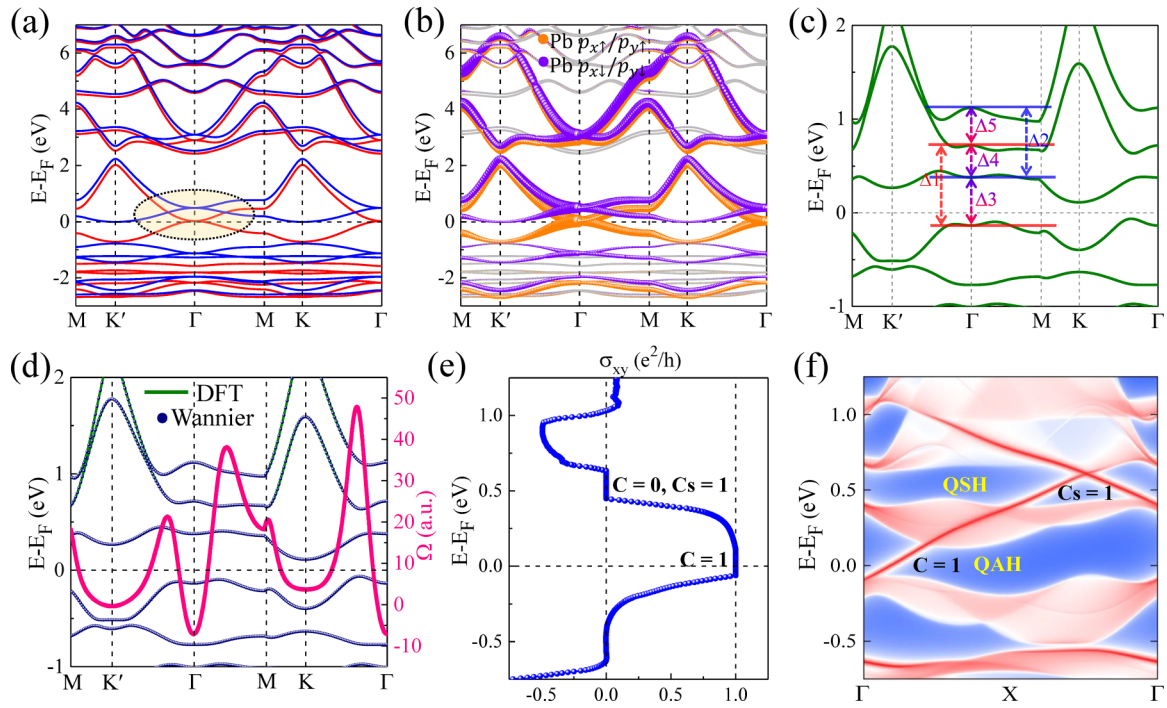

FIG. 3. (a) The spin-polarized band structure of monolayer Pb_2BrO. The red and blue curves denote the spin-up and spin-down bands, respectively. (b) Orbital-resolved band structures of (a), where the contributions from Pb $p_{x\uparrow}/p_{y\uparrow}$ and $p_{x\downarrow}/p_{y\downarrow}$ states to the bands are denoted by orange and violet dots, respectively. (c) The corresponding magnified band structure of panel (a) around the E_F with the consideration of SOC. The characteristic energy gaps ($\Delta 1$ to $\Delta 5$) are marked in panel (c). (d) The SOC band structure for monolayer Pb_2BrO, obtained with DFT methods (olive curves) and Wannier interpolation approaches (navy dots). The pink dots denote the calculated Berry curvatures. (e) The calculated σ_{xy} as a function of the position of E_F. (f) The calculated edge states of the semi-infinite monolayer Pb_2BrO.

$p_{x\uparrow}/p_{y\uparrow}$ and $p_{x\downarrow}/p_{y\downarrow}$ states, respectively. Figure 3(b) clearly illustrates the band structure originating from the 2D honeycomb lattice formed by the Pb atoms with multiple p (p_x and p_y) orbitals in the monolayer Pb_2BrO, which exhibits similarities to the spin-polarized TB band structure depicted in Fig. 1(b). The staggered AB-sublattice potential U is included into the Pb honeycomb lattice due to the nonequivalence of Br and O atoms in the monolayer Pb_2BrO. Additionally, the magnetic exchange field M is introduced into the Pb honeycomb lattice through the magnetization of O atoms. When the SOC is considered, the spin-up and spin-down non-Dirac bands degeneracies at the Γ point are both eliminated, and energy gaps are opened around the Γ point, as shown in Fig. 3(c). Remarkably, the characteristics of the DFT SOC band structure in Fig. 3(c) are consistent with the TB band structure in Fig. 1(c).

In Fig. 3(c), $\Delta 1$ (852.4 meV) and $\Delta 2$ (742.1 meV) are the SOC-induced energy gaps at the Γ point for the spin-up and spin-down non-Dirac degenerate points, respectively. Due to the overlap of $\Delta 1$ and $\Delta 2$, the three typical energy gaps, namely, $\Delta 3$, $\Delta 4$, and $\Delta 5$, which are previously identified in the TB band structure depicted in Fig. 1(c), are now realized in the DFT band structure in Fig. 3(c). Our DFT calculations show that the significant energy gaps $\Delta 3$, $\Delta 4$, and $\Delta 5$ are 512.8, 339.6, and 402.5 meV, respectively. The pink dots in Fig. 3(d) display $\Omega(\mathbf{k})$ calculated using DFT, with E_F positioned within the global insulating state inside $\Delta 3$, showing a similar distribution as illustrated in TB model results in Fig. 1(c). The calculated σ_{xy} presented in Fig. 3(e) confirm that the Chern numbers for the global insulating gaps within $\Delta 3$ and $\Delta 4$ are $C = 1$ and $C = 0$, respectively. In addition, the DFT calculated edge states shown in Fig. 3(f) clearly illustrate the presence of one (spin-up) topologically nontrivial edge states within $\Delta 3$ and two (spin-up and spin-down) within $\Delta 4$, confirming the simultaneously realization of QAH and QSH gaps in the FM monolayer Pb_2BrO. The obtained global QAH and QSH gaps are 175.4 and 187.8 meV, respectively. The E_F in monolayer Pb_2BrO resides within the QAH gap and can be electrically tuned to shift into the QSH gap through gating, thereby enabling switching between these two topologically nontrivial states. The calculated band structures, Chern numbers, and edge states indicate that the remarkable topological states with the coexistence of QAH and QSH gaps in the FM monolayer Pb_2BrO can be described well through our constructed TB model.

As is well known, freestanding 2D monolayer atomic crystals are generally challenging to stabilize. To overcome this challenge, both theoretical [26–28,43] and experimental studies [48,78–80] have demonstrated that epitaxial growth on suitable substrates is an effective strategy to enhance the structural stability and experimental viability of such 2D materials. In our study, we select SiC(0001) and SiO_2(0001) surfaces as representative insulating substrates for supporting the proposed monolayer structure. The built atomic structure of the Pb_2BrO/SiC heterostructure is displayed in Fig. S4(a) in the SM [65]. The bottom and top surfaces of the $\sqrt{3} \times \sqrt{3}$ SiC(0001) substrate are respectively saturated with H and F atoms to remove the dangling-bond states. In our calculations,

the lattice constant of the Pb_2BrO/SiC heterostructure is set at 5.51 Å, which is the average of the lattice constants of the two constituent materials. The calculated band structures and topological edge states presented in Figs. S4(c)– S4(e) in the SM [65] demonstrate that the QAH and QSH gaps still simultaneously exist in the Pb_2BrO/SiC heterostructure. In addition, the atomic structure of the oxygen-functionalized monolayer plumbene grown on the $SiO_2(0001)$ surface, denoted as O-Pb_2/SiO_2, is shown in Fig. S5(a) in the SM [65]. The DFT calculation results given in Figs. S5(c)–S5(h) in the SM [65] illustrate that the QAH and QSH gaps can also be realized simultaneously in the O-Pb_2/SiO_2 heterostructure.

III. CONCLUSIONS

In summary, our comprehensive study combining TB model analysis and first-principles calculations has unveiled the intriguing coexistence of QAH and QSH gaps in 2D honeycomb lattices with non-Dirac bands. Our findings demonstrate that, by introducing a magnetic exchange field and atomic SOC, it is possible to simultaneously open significant QAH and QSH gaps around the non-Dirac Γ point in these systems. The case study of an FM monolayer Pb_2BrO serves as a concrete example, showcasing large QAH and QSH gaps of 175.4 and 187.8 meV, respectively. Notably, E_F in this material resides within the QAH gap and can be electrically tuned to the QSH gap through gating, enabling the reversible switching between these two topologically nontrivial states. These results offer a theoretical foundation for the design of electrically switchable QAH and QSH states in single quantum materials. Our findings demonstrate the versatility of 2D honeycomb lattices with non-Dirac bands as a platform for realizing multifunctional topological states, which hold promise for the development of novel electronic and spintronic devices.

ACKNOWLEDGMENTS

This work was supported by National Natural Science Foundation of China (Grants No. 12474155, No. 11904250, and No. 11747137), Postgraduate Research & Practice Innovation Program of Jiangsu Province (Grant No. KYCX24_-3414), Zhejiang Provincial Natural Science Foundation of China (Grant No. LR25A040001), Ningbo Yongjiang Talent Programme, and Qing Lan Project of Jiangsu Province. The computing for this research was supported by High Performance Computing Platforms at Suzhou University of Science and Technology (Suzhou) and Eastern Institute of Technology (Ningbo).

DATA AVAILABILITY

The data that support the findings of this article are not publicly available upon publication because it is not technically feasible and/or the cost of preparing, depositing, and hosting the data would be prohibitive within the terms of this research project. The data are available from the authors upon reasonable request.

[1] X. L. Qi and S. C. Zhang, The quantum spin Hall effect and topological insulators, Phys. Today **63**(1), 33 (2010).
[2] Y. F. Ren, Z. H. Qiao, and Q. Niu, Topological phases in two-dimensional materials: A review, Rep. Prog. Phys. **79**, 066501 (2016).
[3] C. L. Kane and E. J. Mele, Quantum spin Hall effect in graphene, Phys. Rev. Lett. **95**, 226801 (2005).
[4] B. A. Bernevig, T. L. Hughes, and S. C. Zhang, Quantum spin Hall effect and topological phase transition in HgTe quantum wells, Science **314**, 1757 (2006).
[5] K. He, Y. Y. Wang, and Q. -K. Xue, Quantum anomalous Hall effect, Natl. Sci. Rev. **1**, 38 (2014).
[6] C. Z. Chang, C. X. Liu, and A. H. MacDonald, *Colloquium*: Quantum anomalous Hall effect, Rev. Mod. Phys. **95**, 011002 (2023).
[7] Q. F. Liang, R. Yu, J. Zhou, and X. Hu, Topological states of non-Dirac electrons on a triangular lattice, Phys. Rev. B **93**, 035135 (2016).
[8] J. Y. Zhang, B. Zhao, Y. Xue, T. Zhou, and Z. Q. Yang, Coupling effect of topological states and Chern insulators in two-dimensional triangular lattices, Phys. Rev. B **97**, 125430 (2018).
[9] J. Y. Zhang, B. Zhao, T. Zhou, Y. Xue, Y. Fang, C. L. Ma, and Z. Q. Yang, Topologically trivial states induced by strong spin-orbit coupling and Chern insulators in doped $X(C_{21}N_3H_{15})$ (X = Ta, Hf) metal-organic frameworks, Phys. Rev. B **99**, 035409 (2019).
[10] Z. F. Wang, Z. Liu, and F. Liu, Quantum anomalous Hall effect in 2D organic topological insulators, Phys. Rev. Lett. **110**, 196801 (2013).
[11] F. D. M. Haldane, Model for a quantum Hall effect without Landau levels: Condensed-matter realization of the "parity anomaly," Phys. Rev. Lett. **61**, 2015 (1988).
[12] C. X. Liu, X. L. Qi, X. Dai, Z. Fang, and S. C. Zhang, Quantum anomalous Hall effect in $Hg_{1-y}Mn_yTe$ quantum wells, Phys. Rev. Lett. **101**, 146802 (2008).
[13] Z. H. Qiao, S. A. Yang, W. X. Feng, W. K. Tse, J. Ding, Y. G. Yao, J. Wang, and Q. Niu, Quantum anomalous Hall effect in graphene from Rashba and exchange effects, Phys. Rev. B **82**, 161414(R) (2010).
[14] M. Ezawa, Valley-polarized metals and quantum anomalous Hall effect in silicene, Phys. Rev. Lett. **109**, 055502 (2012).
[15] T. Zhou, J. Y. Zhang, Y. Xue, B. Zhao, H. S. Zhang, H. Jiang, and Z. Q. Yang, Quantum spin-quantum anomalous Hall effect with tunable edge states in Sb monolayer-based heterostructures, Phys. Rev. B **94**, 235449 (2016).
[16] C. C. Liu, W. X. Feng, and Y. G. Yao, Quantum spin Hall effect in silicene and two-dimensional germanium, Phys. Rev. Lett. **107**, 076802 (2011).
[17] Y. Xu, B. H. Yan, H. J. Zhang, J. Wang, G. Xu, P. Tang, W. H. Duan, and S. C. Zhang, Large-gap quantum spin Hall insulators in tin films, Phys. Rev. Lett. **111**, 136804 (2013).

[18] H. M. Weng, X. Dai, and Z. Fang, Transition-metal pentatelluride $ZrTe_5$ and $HfTe_5$: A paradigm for large-gap quantum spin Hall insulators, Phys. Rev. X **4**, 011002 (2014).

[19] Z. G. Song, C. C. Liu, J. B. Yang, J. Z. Han, M. Ye, B. T. Fu, Y. C. Yang, Q. Niu, J. Lu, and Y. G. Yao, Quantum spin Hall insulators and quantum valley Hall insulators of BiX/SbX (X = H, F, Cl and Br) monolayers with a record bulk band gap, NPG Asia Mater **6**, e147 (2014).

[20] X. F. Qian, J. W. Liu, L. Fu, and J. Li, Quantum spin Hall effect in two-dimensional transition metal dichalcogenides, Science **346**, 1344 (2014).

[21] J. J. Zhou, W. X. Feng, C. C. Liu, S. Guan, and Y. G. Yao, Large-gap quantum spin Hall insulator in single layer bismuth monobromide Bi_4Br_4, Nano Lett. **14**, 4767 (2014).

[22] B. Zhao, J. Y. Zhang, W. X. Feng, Y. G. Yao, and Z. Q. Yang, Quantum spin Hall and Z_2 metallic states in an organic material, Phys. Rev. B **90**, 201403(R) (2014).

[23] Y. D. Ma, L. Z. Kou, B. H. Yan, C. W. Niu, Y. Dai, and T. Heine, Two-dimensional inversion-asymmetric topological insulators in functionalized III-Bi bilayers, Phys. Rev. B **91**, 235306 (2015).

[24] T. Zhou, J. Y. Zhang, H. Jiang, I. Žutić, and Z. Q. Yang, Giant spin-Valley polarization and multiple Hall effect in functionalized bismuth monolayers, npj Quantum Mater. **3**, 39 (2018).

[25] T. Zhou, S. Cheng, M. Schleenvoigt, P. Schüffelgen, H. Jiang, Z. Q. Yang, and I. Žutić, Quantum spin-valley Hall kink states: from concept to materials design, Phys. Rev. Lett. **127**, 116402 (2021).

[26] Y. Xu, P. Z. Tang, and S. C. Zhang, Large-gap quantum spin Hall states in decorated stanene grown on a substrate, Phys. Rev. B **92**, 081112(R) (2015).

[27] J. E. Padilha, A. Janotti, A. Fazzio, and A. J. R. da Silva, Substrate-supported large-band-gap quantum spin Hall insulator based on III–V bismuth layers, Phys. Rev. B **94**, 195424 (2016).

[28] H. S. Zhang, Y. Y. Wang, W. J. Yang, J. J. Zhang, X. H. Xu, and F. Liu, Selective substrate-orbital-filtering effect to realize the large-gap quantum spin Hall effect, Nano Lett. **21**, 5828 (2021).

[29] Y. Xia, S. Jin, J. Hu, R. Claessen, W. Hanke, R. Thomale, and G. Li, Band inversion induced large-gap quantum spin Hall states in III-Bi-monolayer/SiO_2, Phys. Rev. B **106**, 165203 (2022).

[30] R. Yu, W. Zhang, H. J. Zhang, S. C. Zhang, X. Dai, and Z. Fang, Quantized anomalous Hall effect in magnetic topological insulators, Science **329**, 61 (2010).

[31] Z. H. Qiao, W. Ren, H. Chen, L. Bellaiche, Z. Y. Zhang, A. H. MacDonald, and Q. Niu, Quantum anomalous Hall effect in graphene proximity coupled to an antiferromagnetic insulator, Phys. Rev. Lett. **112**, 116404 (2014).

[32] J. Y. Zhang, B. Zhao, T. Zhou, Y. Xue, C. L. Ma, and Z. Q. Yang, Strong magnetization and Chern insulators in compressed graphene/CrI_3 van der Waals heterostructures, Phys. Rev. B **97**, 085401 (2018).

[33] J. He, X. Li, P. Lyu, and P. Nachtigall, Near-room-temperature Chern insulator and Dirac spin-gapless semiconductor: nickel chloride monolayer, Nanoscale **9**, 2246 (2017).

[34] C. Huang, J. Zhou, H. Wu, K. Deng, P. Jena, and E. J. Kan, Quantum anomalous Hall effect in ferromagnetic transition metal halides, Phys. Rev. B **95**, 045113 (2017).

[35] Q. Sun and N. Kioussis, Prediction of manganese trihalides as two-dimensional Dirac half-metals, Phys. Rev. B **97**, 094408 (2018).

[36] S. C. Wu, G. C. Shan, and B. H. Yan, Prediction of near-room-temperature quantum anomalous Hall effect on honeycomb materials, Phys. Rev. Lett. **113**, 256401 (2014).

[37] J. Y. You, Z. Zhang, B. Gu, and G. Su, Two-dimensional room-temperature ferromagnetic semiconductors with quantum anomalous Hall effect, Phys. Rev. Appl. **12**, 024063 (2019).

[38] M. H. Zhang, C. W. Zhang, P. J. Wang, and S. S. Li, Prediction of high-temperature Chern insulator with half-metallic edge states in asymmetry-functionalized stanene, Nanoscale **10**, 20226 (2018).

[39] Y. Liang, Y. D. Ma, P. Zhao, H. Wang, B. B. Huang, and Y. Dai, High-temperature quantum anomalous Hall insulator in two-dimensional Bi_2ON, Appl. Phys. Lett. **116**, 162402 (2020).

[40] Z. Y. Li, Y. L. Han, and Z. H. Qiao, Chern number tunable quantum anomalous Hall effect in monolayer transitional metal oxides via manipulating magnetization orientation, Phys. Rev. Lett. **129**, 036801 (2022).

[41] Y. J. Wang, C. C. Lou, B. Zhao, C. L. Ma, and J. Y. Zhang, Doping- and strain-tuned high Curie temperature half-metallicity and quantum anomalous Hall effect in monolayer $NiAl_2S_4$ with non-Dirac and Dirac states, Phys. Rev. B **107**, 085416 (2023).

[42] X. M. Wu, R. H. Li, X. R. Zhou, B. B. Huang, Y. Dai, and C. Niu, Robust quantum anomalous Hall effect with tunable magnetization directions and Chern numbers, Phys. Rev. B **108**, 115438 (2023).

[43] J. C. Shen, J. X. Li, J. H. Qian, X, K. Duan, C. L. Ma, T. Zhou, and J. Y. Zhang, Large-gap non-Dirac quantum anomalous Hall effect in nitride TlSb monolayers on nonmagnetic substrates, Phys. Rev. B **110**, 155423 (2024).

[44] J. Li, Y. Li, S. Du, Z. Wang, B. L. Gu, S. C. Zhang, K. He, W. Duan, and Y. Xu, Intrinsic magnetic topological insulators in van der Waals layered $MnBi_2Te_4$-family materials, Sci. Adv. **5**, eaaw5685 (2019).

[45] D. Q. Zhang, M. J. Shi, T. S. Zhu, D. Y. Xing, H. J. Zhang, and J. Wang, Topological axion states in the magnetic insulator $MnBi_2Te_4$ with the quantized magnetoelectric effect, Phys. Rev. Lett. **122**, 206401 (2019).

[46] M. König, S. Wiedmann, C. Brune, A. Roth, H. Buhmann, L. W. Molenkamp, X. L. Qi, and S. C. Zhang, Quantum spin Hall insulator state in HgTe quantum wells, Science **318**, 766 (2007).

[47] S. F. Wu, V. Fatemi, Q. D. Gibson, K. Watanabe, T. Taniguchi, R. J. Cava, and P. Jarillo-Herrero, Observation of the quantum spin Hall effect up to 100 kelvin in a monolayer crystal, Science **359**, 76 (2018).

[48] F. Reis, G. Li, L. Dudy, M. Bauernfeind, S. Glass, W. Hanke, R. Thomale, J. Schäfer, and R. Claessen, Bismuthene on a SiC substrate: A candidate for a high-temperature quantum spin Hall material, Science **357**, 287 (2017).

[49] C.-Z. Chang, J. S. Zhang, X. Feng, J. Shen, Z. C. Zhang, M. H. Guo, K. Li, Y. B. Ou, P. Wei, L.-L. Wang, Z.-Q. Ji, Y. Feng, S. H. Ji, X. Chen, J. F. Jia, X. Dai, Z. Fang, S.-C. Zhang, K. He, Y. Y. Wang, L. Lu, X.-C. Ma, and Q.-K. Xue, Experimental observation of the quantum anomalous Hall effect in a magnetic topological insulator, Science **340**, 167 (2013).

[50] X. F. Kou, S. T. Guo, Y. B. Fan, L. Pan, M. Lang, Y. Jiang, Q. M. Shao, T. X. Nie, K. Murata, J. S. Tang, Y. Wang, L. He, T. K. Lee, W. L. Lee, and K. L. Wang, Scale-invariant quantum anomalous Hall effect in magnetic topological insulators beyond the two-dimensional limit, Phys. Rev. Lett. **113**, 137201 (2014).

[51] Y. J. Deng, Y. J. Yu, M. Z. Shi, Z. X. Guo, Z. H. Xu, J. Wang, X. H. Chen, and Y. B. Zhang, Quantum anomalous Hall effect in intrinsic magnetic topological insulator $MnBi_2Te_4$, Science **367**, 895 (2020).

[52] M. Serlin, C. L. Tschirhart, H. Polshyn, Y. Zhang, J. Zhu, K. Watanabe, T. Taniguchi, L. Balents, and A. F. Young, Intrinsic quantized anomalous Hall effect in a moiré heterostructure, Science **367**, 900 (2020).

[53] Z. G. Lu, T. H. Han, Y. X. Yao, A. P. Reddy, J. X. Yang, J. Seo, K. Watanabe, T. Taniguchi, L. Fu, and L. Ju, Fractional quantum anomalous Hall effect in multilayer graphene, Nature (London) **626**, 759 (2024).

[54] J. Q. Cai, E. Anderson, C. Wang, X. W. Zhang, X. Y. Liu, W. Holtzmann, Y. Zhang, F. R. Fan, T. Taniguchi, K. Watanabe, Y. Ran, T. Cao, L. Fu, D. Xiao, W. Yao, and X. D. Xu, Signatures of fractional quantum anomalous Hall states in twisted $MoTe_2$, Nature (London) **622**, 63 (2023).

[55] F. Xu, Z. Sun, T. T. Jia, C. Liu, C. Xu, C. S. Li, Y. Gu, K. Watanabe, T. Taniguchi, B. B. Tong, J. F. Jia, Z. W. Shi, S. W. Jiang, Y. Zhang, X. X. Liu, and T. X. Li, Observation of integer and fractional quantum anomalous Hall effects in twisted bilayer $MoTe_2$, Phys. Rev. X **13**, 031037 (2023).

[56] E. Prodan, Robustness of the spin-Chern number, Phys. Rev. B **80**, 125327 (2009).

[57] Y. Y. Yang, Z. Xu, L. Sheng, B. G. Wang, D. Y. Xing, and D. N. Sheng, Time-reversal-symmetry-broken quantum spin Hall effect, Phys. Rev. Lett. **107**, 066602 (2011).

[58] M. Ezawa, Spin valleytronics in silicene: Quantum spin-Hall quantum anomalous Hall insulators and single-valley semimetals, Phys. Rev. B **87**, 155415 (2013).

[59] F. Zhang, J. Jung, G. A. Fiete, Q. Niu, and A. H. MacDonald, Spontaneous quantum Hall states in chirally stacked few-layer graphene systems, Phys. Rev. Lett. **106**, 156801 (2011).

[60] T. Zhou, J. Y. Zhang, B. Zhao, H. S. Zhang, and Z. Q. Yang, Quantum spin-quantum anomalous Hall insulators and topological transitions in functionalized Sb(111) monolayers, Nano Lett. **15**, 5149 (2015).

[61] M. Q. Sui, G. R. Chen, L. G. Ma, W. Y. Shan, D. Tian, K. Watanabe, T. Taniguchi, X. F. Jin, W. Yao, D. Xiao, and Y. B. Zhang, Gate-tunable topological valley transport in bilayer graphene, Nat. Phys. **11**, 1027 (2015).

[62] A. Dankert and S. P. Dash, Electrical gate control of spin current in van der Waals heterostructures at room temperature, Nat. Commun. **8**, 16093 (2017).

[63] X. K. Duan, J. Y. Zhang, Z. Y. Zhu, Y. T. Liu, Z. Y. Zhang, I. Žutić, and T. Zhou, Antiferroelectric altermagnets: Antiferroelectricity alters magnets, Phys. Rev. Lett. **134**, 106801 (2025).

[64] Z. Y. Zhu, X. K. Duan, J. Y. Zhang, B. W. Hao, I. Žutić, and T. Zhou, Two-dimensional ferroelectric altermagnets: From model to material realization, Nano Letters (2025), doi:10.1021/acs.nanolett.5c02121.

[65] See Supplemental Material at http://link.aps.org/supplemental/10.1103/PhysRevB.111.235414 for detailed information about the band structures and topological properties of the construct TB model in the absence of an exchange field ($M = 0.0$ eV); the band structures and topological properties of the construct TB model when considering a large exchange field ($M = 1.20$ eV); and the atomic structures, band structures, and topological edge states of the Pb_2BrO/SiC and O-Pb_2/SiO_2 heterostructures.

[66] D. J. Thouless, M. Kohmoto, M. P. Nightingale, and M. den Nijs, Quantized Hall conductance in a two-dimensional periodic potential, Phys. Rev. Lett. **49**, 405 (1982).

[67] Y. G. Yao, L. Kleinman, A. H. MacDonald, J. Sinova, T. Jungwirth, D. S. Wang, E. Wang, and Q. Niu, First principles calculation of anomalous Hall conductivity in ferromagnetic bcc Fe, Phys. Rev. Lett. **92**, 037204 (2004).

[68] P. E. Blöchl, Projector augmented-wave method, Phys. Rev. B **50**, 17953 (1994).

[69] G. Kresse and J. Furthmüller, Efficient iterative schemes for *ab initio* total-energy calculations using a plane-wave basis set, Phys. Rev. B **54**, 11169 (1996).

[70] J. P. Perdew, K. Burke, and M. Ernzerhof, Generalized gradient approximation made simple, Phys. Rev. Lett. **77**, 3865 (1996).

[71] N. Marzari and D. Vanderbilt, Maximally localized generalized Wannier functions for composite energy bands, Phys. Rev. B **56**, 12847 (1997).

[72] I. Souza, N. Marzari, and D. Vanderbilt, Maximally localized Wannier functions for entangled energy bands, Phys. Rev. B **65**, 035109 (2001).

[73] A. A. Mostofi, J. R. Yates, Y. S. Lee, I. Souza, D. Vanderbilt, and N. Marzari, Wannier90: A tool for obtaining maximally localized Wannier functions, Comput. Phys. Commun. **178**, 685 (2008).

[74] X. J. Wang, J. R. Yates, I. Souza, and D. Vanderbilt, *Ab initio* calculation of the anomalous Hall conductivity by Wannier interpolation, Phys. Rev. B **74**, 195118 (2006).

[75] Q. S. Wu, S. Zhang, H. F. Song, M. Troyer, and A. A. Soluyanov, WannierTools: An open-source software package for novel topological materials, Comput. Phys. Commun. **224**, 405 (2018).

[76] L. M. Zhang, J. W. Yu, M. M. Yang, Q. Xie, H. L. Peng, and Z. F. Liu, Janus graphene from asymmetric two-dimensional chemistry, Nat. Commun. **4**, 1443 (2013).

[77] W. B. Zhang, Q. Qu, P. Zhu, and C. H. Lam, Robust intrinsic ferromagnetism and half semiconductivity in stable two-dimensional single-layer chromium trihalides, J. Mater. Chem. C **3**, 12457 (2015).

[78] J. Yuhara, B. He, N. Matsunami, M. Nakatake, and G. Le Lay, Graphene's latest cousin: Plumbene epitaxial growth on a "nano WaterCube," Adv. Mater. **31**, 1901017 (2019).

[79] P. Bampoulis, C. Castenmiller, D. J. Klaassen, J. van Mil, Y. Liu, C. C. Liu, Y. G. Yao, M. Ezawa, A. N. Rudenko, and H. J. W. Zandvliet, Quantum spin Hall states and topological phase transition in germanene, Phys. Rev. Lett. **130**, 196401 (2023).

[80] L. Tao, E. Cinquanta, D. Chiappe, C. Grazianetti, M. Fanciulli, M. Dubey, A. Molle, and D. Akinwande, Silicene field-effect transistors operating at room temperature, Nat. Nanotechnol. **10**, 227 (2015).